

**NASA TECHNICAL NOTE**



**NASA TN D-5132**

*c.1*

NASA TN D-5132



LOAN COPY: RETURN TO  
AFWL (WLIL-2)  
KIRTLAND AFB, N MEX

# VISCOUS FLOW IN A SHORT CYLINDRICAL VORTEX CHAMBER WITH A FINITE SWIRL RATIO

*by Robert W. Hornbeck*

*Lewis Research Center*

*Cleveland, Ohio*



VISCOUS FLOW IN A SHORT CYLINDRICAL VORTEX  
CHAMBER WITH A FINITE SWIRL RATIO

By Robert W. Hornbeck

Lewis Research Center  
Cleveland, Ohio

NATIONAL AERONAUTICS AND SPACE ADMINISTRATION

---

For sale by the Clearinghouse for Federal Scientific and Technical Information  
Springfield, Virginia 22151 - CFSTI price \$3.00

## ABSTRACT

The laminar incompressible viscous flow in a short cylindrical vortex chamber is analyzed numerically. The flow is assumed to enter the chamber periphery with an arbitrary ratio of tangential to radial velocity components and to exit at a line sink at the chamber axis. The numerical technique permits consideration of both the tangential and radial momentum equations. Comparisons are made with solutions available for the limiting cases of zero swirl and infinite swirl. Results are presented for a wide variety of swirl ratios, Reynolds numbers, and chamber aspect ratios. The results include radial and tangential velocity profiles, pressure distributions, and points of radial flow reversal.

# VISCOUS FLOW IN A SHORT CYLINDRICAL VORTEX CHAMBER WITH A FINITE SWIRL RATIO

by Robert W. Hornbeck  
Lewis Research Center

## SUMMARY

The problem of laminar incompressible viscous flow in a short cylindrical vortex chamber is analyzed using a numerical technique. This technique permits the consideration of both the tangential and radial momentum equations as well as continuity, hence, the amount of swirl introduced into the flow at the periphery of the chamber may be varied. Velocity profiles and pressure distributions are obtained, assuming that the radial- and tangential-velocity distributions at the peripheral inlet to the chamber are uniform across the height. Values of Reynolds number  $Re$  based on the radial inlet velocity and chamber height between 20 and 2000 are considered. The swirl ratio  $S$ , defined as the ratio of tangential to radial inlet velocity, is varied from 0 to 50. Two values of chamber radius to chamber half-height ( $R_1 = 5$  and 10) are considered.

Overshoots in the radial velocity within the end-wall boundary layers are found to occur somewhere in the chamber for all  $S > 1$ , and this overshoot (an increase in the radial velocity in the boundary layer over the velocity in the region far from the wall) is increased for increasing swirl and decreasing distance from the central axis of the chamber. For large values of  $Re$ , the end-wall boundary layers are very thin; hence the radial velocity distributions show sharp spikes in the boundary layer and are relatively uniform over the remaining channel height. For small  $Re$ , the end-wall boundary layers are sufficiently thick to fill the chamber height, except for the region close to the peripheral inlet.

For sufficiently high swirl ratios (greater than about 4 for most cases considered) a local reversal in the radial velocity will occur at some value of the radius, on the chamber centerplane. When this radial outflow occurs, the numerical scheme becomes unstable and must be terminated at the radius at which it occurs.

The pressure distributions are found to be virtually identical to the potential flow distributions for  $S > 1$ , but are dependent on  $Re$  and  $R_1$  for  $S \leq 1$ . Even small amounts of swirl are found to have a relatively significant effect on the pressure drop between any two radial stations in the chamber.

## INTRODUCTION

Considerable work has been done in recent years toward the description of flow in a confined vortex. A typical confined vortex configuration might consist of a cylindrical chamber with a fluid injected both radially and tangentially at the chamber periphery and withdrawn at the central axis. The work has been motivated at least partly by interest in a number of devices that utilize such a vortex configuration, including the Ranque-Hilsch tube, the magnetohydrodynamic vortex generator, the vortex nuclear reactor and, most recently, the vortex amplifier for fluidics applications. An excellent historical review of the vortex literature is given in Anderson (ref. 1). Reference 1 represents the most accurate solution to date for the velocity and temperature distributions inside a vortex chamber, but it is restricted to very high swirl so that the radial inflow velocity is negligible compared with the tangential (swirl) velocity in the stream between the end-wall boundary layers. Numerical solutions are then obtained assuming that the free stream is either irrotational or in solid-body rotation.

The influence of various swirl ratios was investigated experimentally by Donaldson and Snedeker (ref. 2) but only for a cylindrical vortex chamber with a single end wall, rather than the fully confined vortex. In a recent analysis by Ostrach and Loper (ref. 3), finite swirl ratios were considered for the confined vortex, but it was necessary to linearize the basic equations in such a way as to ignore the effect of swirl ratio on the boundary-layer thickness. The present analysis retains the essential nonlinearities of the basic equations and accurately accounts for all of the effects of swirl ratio.

Savino and Keshock have presented the most reliable experimental work to date on the radial and tangential velocity distributions in a confined vortex (ref. 4). Although the flow was turbulent, this investigation allows at least a qualitative comparison with the work of Anderson (ref. 1) and the present study for the case of high swirl ratios ( $>15$ ).

In the present investigation, viscous incompressible flow in a confined vortex is analyzed by using a numerical marching technique that permits full consideration of both tangential and radial momentum at all points in the chamber, thus allowing consideration of any swirl ratio, as well as viscous effects over the entire chamber. In order to employ a numerical marching technique, it is necessary to drop certain terms in the basic equations. This restricts the solution to short vortex chambers (chambers in which the radius is larger than the height). One drawback to the use of this numerical scheme is that the numerical technique becomes unstable when radial outflow is present. As a result of this, the solution may only be carried inward from the periphery of the chamber until radial outflow begins to occur. Despite this shortcoming, the method does permit the detailed study of a large number of interesting cases, particularly since the real area of interest in this investigation is for finite swirl ratios, where radial outflow is less likely to occur.

## PROBLEM AND BASIC EQUATIONS

The problem configuration for a typical short vortex chamber is shown in figure 1. The fluid is assumed to enter the chamber both radially and tangentially with velocity distributions that are uniform over the height of the chamber. The flow is assumed to be laminar and incompressible, with constant properties. The fluid is removed at the center of the channel by what is assumed to be a line sink. In the actual chamber, central exit tubes of relatively small diameter must be provided at the top and bottom of the chamber. These, presumably, will not have a large effect on the flow pattern in the chamber except close to the center. Axial symmetry is assumed throughout.

The basic equations of motion for the steady flow of an incompressible, constant property fluid in cylindrical coordinates are  
r-direction momentum:

$$\rho \left( w \frac{\partial u}{\partial z} + u \frac{\partial u}{\partial r} - \frac{v^2}{r} \right) = - \frac{dp}{dr} + \mu \left( \frac{\partial^2 u}{\partial z^2} + \frac{\partial^2 u}{\partial r^2} + \frac{1}{r} \frac{\partial u}{\partial r} - \frac{u}{r^2} \right) \quad (1)$$

$\theta$ -direction momentum:

$$\rho \left( w \frac{\partial v}{\partial z} + u \frac{\partial v}{\partial r} + \frac{uv}{r} \right) = \mu \left( \frac{\partial^2 v}{\partial z^2} + \frac{\partial^2 v}{\partial r^2} + \frac{1}{r} \frac{\partial v}{\partial r} - \frac{v}{r^2} \right) \quad (2)$$

continuity:

$$\frac{\partial w}{\partial z} + \frac{1}{r} \frac{\partial(ur)}{\partial r} = 0 \quad (3)$$

When an order of magnitude analysis is made and terms of  $\theta$  ( $h^2/r_1^2$ ) are neglected, the basic equations are reduced to

r-direction momentum:

$$\rho \left( w \frac{\partial u}{\partial z} + u \frac{\partial u}{\partial r} - \frac{v^2}{r} \right) = - \frac{dp}{dr} + \mu \left( \frac{\partial^2 u}{\partial z^2} \right) \quad (4)$$

$\theta$ -direction momentum:

$$\rho \left( w \frac{\partial v}{\partial z} + u \frac{\partial v}{\partial r} + \frac{uv}{r} \right) = \mu \left( \frac{\partial^2 v}{\partial z^2} \right) \quad (5)$$

continuity:

$$\frac{\partial w}{\partial z} + \frac{1}{r} \frac{\partial(ur)}{\partial r} = 0 \quad (6)$$

Equations (4) to (6) apply only for small  $(h/r_1)$ , that is, short vortex chambers. The boundary conditions on equations (4) to (6) are

$$\left. \begin{aligned} u(r_1, z) &= -u_1 = \text{Constant} \\ u(r, h) &= 0 \\ \frac{\partial u}{\partial z}(r, 0) &= 0 \\ v(r_1, z) &= v_1 = \text{Constant} \\ v(r, h) &= 0 \\ \frac{\partial v}{\partial z}(r, 0) &= 0 \\ w(r, h) &= 0 \\ w(r, 0) &= 0 \end{aligned} \right\} \quad (7)$$

In order to attempt a numerical solution, it is first necessary to put the basic equations into a dimensionless form which reduces the number of parameters that appear to a minimum. The dimensionless variables chosen are

$$\left. \begin{aligned}
 U &= \frac{u}{u_1} \\
 V &= \frac{v}{u_1} \\
 W &= \frac{w}{u_1} \\
 P &= \frac{p - p_1}{\rho u_1^2} \\
 Z &= \frac{z}{h} \\
 R &= \frac{r}{h}
 \end{aligned} \right\} \quad (8)$$

Inserting the dimensionless variables (8) into equations (4) to (6) results in the following dimensionless forms of the basic equations:

$$W \frac{\partial U}{\partial Z} + U \frac{\partial U}{\partial R} - \frac{V^2}{R} = - \frac{dP}{dR} + \frac{1}{Re} \frac{\partial^2 U}{\partial Z^2} \quad (9)$$

$$W \frac{\partial V}{\partial Z} + U \frac{\partial V}{\partial R} + \frac{UV}{R} = \frac{1}{Re} \frac{\partial^2 V}{\partial Z^2} \quad (10)$$

$$\frac{\partial W}{\partial Z} + \frac{1}{R} \frac{\partial (UR)}{\partial R} = 0 \quad (11)$$

where  $Re = \rho u_1 h / \mu$  is a Reynolds number based on the channel height. This parameter is a natural result of the dimensionless variables chosen earlier. The boundary conditions (7) in dimensionless form become



$$\left. \begin{aligned}
 U(R_1, Z) &= -1 \\
 U(R, 1) &= 0 \\
 \frac{\partial U}{\partial Z}(R, 0) &= 0 \\
 V(R_1, Z) &= \frac{v_1}{u_1} = S \\
 V(R, 1) &= 0 \\
 \frac{\partial V}{\partial Z}(R, 0) &= 0 \\
 W(R, 1) &= 0 \\
 W(R, 0) &= 0
 \end{aligned} \right\} \quad (12)$$

where

$$R_1 = \frac{r_1}{h}$$

The parameters (including boundary conditions) that must be considered for this problem are a geometry parameter  $r_1/h$ , the swirl ratio  $v_1/u_1$ , and the Reynolds number  $\rho u_1 h / \mu$ .

### Finite Difference Representation

The finite difference grid employed in this analysis is shown in figure 2. Note that increasing  $j$  subscript corresponds to decreasing radius, since the marching direction will be from the outside of the chamber toward the center. Equations (9) to (11) will now be expressed in an implicit finite difference representation at a point  $(j + 1, k)$ :

$$\begin{aligned}
W_{j,k} \frac{U_{j+1,k+1} - U_{j+1,k-1}}{2 \Delta Z} + U_{j,k} \frac{U_{j,k} - U_{j+1,k}}{\Delta R} - \frac{V_{j,k} V_{j+1,k}}{R_{j+1}} \\
= - \frac{P_j - P_{j+1}}{\Delta R} + \frac{1}{\text{Re}} \left[ \frac{U_{j+1,k+1} - 2U_{j+1,k} + U_{j+1,k-1}}{(\Delta Z)^2} \right] \quad (13)
\end{aligned}$$

$$\begin{aligned}
W_{j,k} \frac{V_{j+1,k+1} - V_{j+1,k-1}}{2 \Delta Z} + U_{j,k} \frac{V_{j,k} - V_{j+1,k}}{\Delta R} + \frac{V_{j+1,k} U_{j,k}}{R_{j+1}} \\
= \frac{1}{\text{Re}} \left[ \frac{V_{j+1,k+1} - 2V_{j+1,k} + V_{j+1,k-1}}{(\Delta Z)^2} \right] \quad (14)
\end{aligned}$$

$$\frac{W_{j+1,k+1} - W_{j+1,k}}{\Delta Z} + \frac{1}{R_{j+1}} \left[ \frac{U_{j,k} R_j - U_{j+1,k} R_{j+1}}{\Delta R} \right] = 0 \quad (15)$$

Equations (13) to (15), written for  $k = 0(1)n$  (i.e., for  $k$  ranging from 0 to  $n$  in steps of 1), constitute a complete set of  $(3n + 3)$  equations in the  $(3n + 3)$  unknowns

$U_{j+1,0}, \dots, U_{j+1,n}; V_{j+1,0}, \dots, V_{j+1,n}; W_{j+1,1}, \dots, W_{j+1,n};$  and  $P_{j+1}$ .

### Method of Solution

In order to obtain a solution to equations (13) to (15), the first step will be to rearrange equations (13) and (14) into a more useful form. Equation (13) becomes

$$\begin{aligned}
\left[ \frac{-W_{j,k}}{2(\Delta Z)} - \frac{1}{\text{Re}(\Delta Z)^2} \right] U_{j+1,k-1} + \left[ \frac{-U_{j,k}}{\Delta R} + \frac{2}{\text{Re}(\Delta Z)^2} \right] U_{j+1,k} + \left[ \frac{W_{j,k}}{2(\Delta Z)} - \frac{1}{\text{Re}(\Delta Z)^2} \right] U_{j+1,k+1} \\
+ \left[ \frac{-V_{j,k}}{R_{j+1}} \right] V_{j+1,k} + \left[ \frac{-1}{\Delta R} \right] P_{j+1} = \frac{-U_{j,k}^2}{\Delta R} - \frac{P_j}{\Delta R} \quad (16)
\end{aligned}$$

Equation (14) becomes

$$\left[ \frac{-W_{j,k}}{2(\Delta Z)} - \frac{1}{\text{Re}(\Delta Z)^2} \right] V_{j+1,k-1} + \left[ \frac{-U_{j,k}}{\Delta R} + \frac{U_{j,k}}{R_{j+1}} + \frac{2}{\text{Re}(\Delta Z)^2} \right] V_{j+1,k} + \left[ \frac{W_{j,k}}{2(\Delta Z)} - \frac{1}{\text{Re}(\Delta Z)^2} \right] V_{j+1,k+1} = \frac{-U_{j,k} V_{j,k}}{\Delta R} \quad (17)$$

Equations (16) and (17) for  $k = 0(1)n$  comprise  $(2n + 2)$  equations in the  $(2n + 3)$  unknowns  $U_{j+1,0}, \dots, U_{j+1,n}; V_{j+1,0}, \dots, V_{j+1,n};$  and  $P_{j+1}$ . Rather than employing the continuity difference equation (15) to complete the set thus introducing the  $W_{j+1,k}$ 's as additional unknowns, it is advantageous to introduce the integral form of continuity

$$2\pi R_{j+1} \left( \int_0^1 U dZ \Big|_{j+1} \right) = 2\pi R_j \left( \int_0^1 U dZ \Big|_j \right) = 2\pi R_1$$

Equation (18) may be written in finite difference form as

$$\left( U_{j+1,0} + 2 \sum_{k=1}^n U_{j+1,k} \right) \frac{\Delta Z}{2} = \frac{R_1}{R_{j+1}} \quad (19)$$

Equation (19) together with equations (16) and (17) written for  $k = 0(1)n$  now completes the set of  $(2n + 3)$  equations in the  $(2n + 3)$  unknowns  $U_{j+1,0}, \dots, U_{j+1,n}; V_{j+1,0}, \dots, V_{j+1,n};$  and  $P_{j+1}$ . This is a significant reduction in number from the  $(3n + 3)$  equations which it would be necessary to solve if the continuity difference equation (15) were used. The use of an integral continuity equation of this type in finite difference analyses of confined flow problems was apparently first used by Bodoia and Osterle (ref. 5), and the techniques used herein have their foundations in that work and in the work of Hornbeck, Rouleau, and Osterle (ref. 6) in which two momentum equations and continuity were solved simultaneously for the entrance flow in a porous tube.

The complete set of equations may be written in matrix form as

$\beta_0$	$\gamma_0$					$\psi_0$							$\eta$	$U_{j+1,0}$	$\varphi_0$
$\alpha_1$	$\beta_1$	$\gamma_1$				$\psi_1$							$\eta$	$U_{j+1,1}$	$\varphi_1$
	$\alpha_2$	$\beta_2$	$\gamma_2$			$\psi_2$							$\eta$	$U_{j+1,2}$	$\varphi_2$
						$\alpha_{n-1}$	$\beta_{n-1}$	$\gamma_{n-1}$					$\eta$	$U_{j+1,n-1}$	$\varphi_{n-1}$
							$\alpha_n$	$\beta_n$					$\eta$	$U_{j+1,n}$	$\varphi_n$
													$0 \times$	$V_{j+1,0}$	$= F_0$
							$B_0$	$G_0$					$0$	$V_{j+1,1}$	$F_1$
							$A_1$	$B_1$	$G_1$				$0$	$V_{j+1,2}$	$F_2$
								$A_2$	$B_2$	$G_2$			$0$		
													$0$		
													$0$	$V_{j+1,n-1}$	$F_{n-1}$
													$0$	$V_{j+1,n}$	$F_n$
$1$	$2$	$2$	$-$	$-$	$2$	$2$	$0$	$0$	$0$	$0$	$0$	$0$	$0$	$0$	$Q$

(20)

where

$$\beta_0 = \frac{-U_{j,0}}{\Delta R} + \frac{2}{\text{Re}(\Delta Z)^2}$$

$$\gamma_0 = \frac{-2}{\text{Re}(\Delta Z)^2}$$

$$\eta = \frac{-1}{\Delta R}$$

$$\alpha_k = \frac{-W_{j,k}}{2(\Delta Z)} - \frac{1}{\text{Re}(\Delta Z)^2} \quad (k \neq 0)$$

$$\beta_k = \frac{-U_{j,k}}{\Delta R} + \frac{2}{\text{Re}(\Delta Z)^2} \quad (k \neq 0)$$

$$\gamma_k = \frac{W_{j,k}}{2(\Delta Z)} - \frac{1}{\text{Re}(\Delta Z)^2} \quad (k \neq 0)$$

$$\psi_k = -\frac{V_{j,k}}{R_{j+1}}$$

$$\phi_k = \frac{-U_{j,k}^2 - P_j}{\Delta R}$$

$$B_0 = \frac{-U_{j,0}}{\Delta R} + \frac{U_{j,0}}{R_{j+1}} + \frac{2}{\text{Re}(\Delta Z)^2}$$

$$G_0 = -\frac{2}{\text{Re}(\Delta Z)^2}$$

$$A_k = -\frac{W_{j,k}}{2(\Delta Z)} - \frac{1}{\text{Re}(\Delta Z)^2} \quad (k \neq 0)$$

$$B_k = -\frac{U_{j,k}}{\Delta R} + \frac{U_{j,k}}{R_{j+1}} + \frac{2}{\text{Re}(\Delta Z)^2} \quad (k \neq 0)$$

$$G_k = \frac{W_{j,k}}{2(\Delta Z)} - \frac{1}{\text{Re}(\Delta Z)^2} \quad (k \neq 0)$$

$$F_k = -\frac{U_{j,k} V_{j,k}}{\Delta R}$$

$$Q = \frac{2R_1}{(\Delta Z)R_{j+1}}$$

The symmetry conditions have been included in equation (20) for  $k = 0$ .

The solution to equation (20) may be obtained by any of the standard methods used for simultaneous linear equation solutions, such as Gaussian elimination, a modification of Gauss-Seidel iteration, or inverting the coefficient matrix and multiplying the right hand side column vector by the inverse.

Once the solution to the set of equations has been obtained, it will be necessary to obtain the values  $W_{i+1,1}, \dots, W_{i+1,n}$  before proceeding. This may be readily accomplished by solving equation (15) for  $W_{j+1,k+1}$ , yielding

$$W_{j+1,k+1} = W_{j+1,k} - \frac{\Delta Z}{(\Delta R)(R_{j+1})} \left[ U_{j,k} R_j - U_{j+1,k} R_{j+1} \right] \quad (21)$$

This solution for  $W_{j+1,k+1}$  may be simply advanced in the direction of increasing  $k$ , starting from  $k = 0$  and proceeding step by step.

After all values of  $U_{j+1,k}$ ,  $V_{j+1,k}$ ,  $W_{j+1,k}$ , and  $P_{j+1}$  have been found, another step  $\Delta R$  inward along the radius may be taken and the entire process repeated.

Because of the computational difficulties that occur when the boundary layers are very thin and the velocity gradients high, it is advantageous to use a considerably smaller  $\Delta Z$  mesh close to the wall than that used toward the midplane of the chamber. The details of the method used for changing the mesh size are given in references 7 and 8.

## RESULTS AND DISCUSSION

The equations derived in the previous section were solved on a high-speed digital computer. The axial mesh sizes used were  $\Delta Z = 0.1$  toward the chamber centerplane and  $\Delta Z = 0.015$  in the region close to the walls, that is,  $Z > 0.7$ . For a few of the high Reynolds number cases where the boundary layers were very thin, it was necessary to, instead, use  $\Delta Z = 0.005$  for  $Z > 0.9$  and  $\Delta Z = 0.1$  for  $Z < 0.9$ . The radial mesh sizes used were  $\Delta R = 0.025$  for the  $R_1 = 5$  cases and  $\Delta R = 0.05$  for the  $R_1 = 10$  cases.

The results presented include radial- and tangential-velocity profiles and pressure distributions. The values of parameters considered include  $R_1 = 5$  and 10;  $Re = 15, 20, 50, 200,$  and 2000; and  $S = 0.2, 0.5, 0.75, 1, 2, 4, 10,$  and 50. A rather detailed presentation of radial-velocity distributions is given for  $S \geq 1$ , but only a few representative tangential-velocity profiles are shown because of the general similarity of these profiles. Pressure distributions are illustrated for the full range of parameters. Also included is a graph of the radii at which radial flow reversal takes place as a function of swirl ratio and Reynolds number, and a set of comparisons with existing

solutions.

Figure 3 compares the profiles of the radial velocity component obtained in this investigation with those obtained by Anderson (ref. 1) for very high swirl. Anderson's profiles were derived for two types of imposed rotational motion in the flow region outside the end-wall boundary layer: (1) irrotational vortex motion and (2) solid-body rotation. Anderson's profiles revealed a tendency for a small magnitude flow reversal to develop only when the main stream was in a solid-body rotational mode. This reversal occurred near the outside diameter of the chamber in the region  $0.8 < R/R_1 < 1.0$ . With the irrotational vortex motion case, Anderson found no tendency for the development of flow reversal.

Typical radial velocity profiles obtained by Anderson and from the present numerical solution are compared in highly magnified form in figure 3(a) for  $Re = 15$  and  $S = 20$ . For these conditions, the irrotational and solid-body rotation solutions of Anderson are quite similar, and the solution obtained in the present investigation lies between the two and favorably agrees with both of the profiles in general shape and location of the peak. The agreement is best with the irrotational vortex-solution profile. The low Reynolds number solutions obtained in the present investigation behave in a qualitative way like the solid-body rotation solutions of Anderson, in that they show a distinct tendency to flow reversal quite close to the chamber periphery. The value of  $S = 20$ , which was used to obtain the results shown in figure 3(a) for the present investigation, was the largest value of swirl ratio that could be used for  $Re = 15$  and still allow the radial position  $R = 9$  to be reached without reversal.

Figure 3(b) shows a comparison of the solution obtained from the present investigation with the solutions of Anderson for  $Re = 2000$  and  $S = 50$ . The profiles are very highly magnified and the agreement of the present solution with the irrotational vortex solution is excellent. The small discrepancies that are present are caused at least partly by the fact that there is always some radial forced flow in the present investigation, whereas any radial flow present in Anderson's solution is entirely induced flow. This results in a somewhat higher radial flow rate for the results of the present investigation. This discrepancy would tend to decrease with increasing swirl ratio. The solid-body rotation solution does not give good agreement with the present solution. The profile shown for the solid-body rotation solution has reversed at the chamber centerplane, but the profile from the present solution shows no tendency toward flow reversal at this high Reynolds number and differs significantly in the shape and magnitude of the peak from the solid-body rotation solution.

The present investigation thus yields solutions that fall somewhere between the irrotational vortex and solid-body rotation solutions of Anderson, with some characteristics of both. The best agreement over the entire range of parameters appears to be with the irrotational vortex solution. Further evidence that the vortex flow outside of

the end-wall boundary layers is essentially irrotational may be found later in this report in the discussion of tangential-velocity profiles.

Figure 4 compares results of the present investigation and those of two other investigations for the radial pressure distribution with no swirl, that is, radial convergent flow between parallel plates. The solutions used for comparison are those of Moller (ref. 9) and Comolet (ref. 10). Results identical with those of Comolet were also found independently by Levesey (ref. 11). These analyses are momentum integral solutions in which some form of parabolic velocity profile is assumed. The agreement of the present numerical solution with the integral solutions is quite good. The numerical solution agrees very well with that of Moller for  $R \geq 3$  and with that of Comolet for  $R < 3$ . In the region  $R > 5$ , the pressure drop of the present solution is higher than that obtained from either of the integral solutions, which is due at least in part to the higher pressure drop that results from the uniform inlet velocity profile used in the present analysis as opposed to the parabolic profile employed in the other investigations.

A solution including inertia for zero swirl flow between parallel plates was carried out by Peube (ref. 12) using a series expansion, but, for the values of parameters considered herein, the truncated form of the expansion given by Peube is not adequate, and presumably many more terms would be required for reasonable accuracy. No comparison, therefore, will be made with this solution.

Figure 5 shows radial velocity distributions for Reynolds numbers of 50, 200, and 2000. For each Reynolds number, values of  $R_1$  of 5 and 10 are considered. The swirl ratio  $S$  appears on each graph as a parameter that varies from 1 to 50 for  $Re = 50$ , from 1 to 10 for  $Re = 200$ , and from 1 to 4 for  $Re = 2000$ . Larger values for the upper limit of  $S$  for  $Re = 200$  and  $Re = 2000$  were not felt to be practical since the corresponding Reynolds number based on the tangential velocity would exceed any reasonable limit for laminar flow.

Figure 5(a) illustrates the radial-velocity overshoot in the boundary layer, which is the most striking characteristic of vortex flow. The higher the swirl ratio, the greater the tendency toward this overshoot, while the radial velocity near the chamber centerplane is correspondingly decreased. This effect is also accentuated as the axis of the chamber is approached as may be seen by comparing figures 5(a-1) and (a-2). This overshoot phenomenon is caused by the tangential velocity decreasing rapidly in the boundary-layer region, which reduces the centrifugal effect in that region and allows the radial pressure gradient to drive the flow inward along the chamber wall.

The end-wall boundary-layer thickness is an inverse function of the Reynolds number, and, for  $Re = 50$  and  $R_1 = 10$  in (fig. 5(a-1)), the boundary layers have reached almost halfway to the chamber centerplane at only one-tenth of the distance from the periphery to the axis of the chamber.



One significant result of the swirl is that, for even moderately high swirl ratios ( $S \geq 4$ ), a significant portion of the radial flow is carried in the boundary layers close to the end walls. For example, in figure 5(a-2) we find that for  $S = 4$  about one-third of the total radial flow is confined to the region between  $Z = 0.8$  and the end wall when a radial position  $R = 5$  halfway to the chamber axis has been reached.

Figures 5(a-3) and (a-4) show results for the same Reynolds number of 50 used to obtain the results shown in figures 5(a-1) and (a-2) but for a chamber with a smaller dimensionless radius  $R_1 = 5$ . The boundary layers occupy a slightly smaller fraction of the total chamber height for the  $R_1 = 5$  cases than for the  $R_1 = 10$  cases at the same relative radial location  $R/R_1$  when all other parameters are held constant. This seems to be the only significant effect of varying  $R_1$ .

Figure 5(b) shows a set of radial-velocity profiles with  $Re = 200$  and  $R_1 = 10$  and 5. These results differ from those for the  $Re = 50$  cases, primarily in the effect of boundary-layer thickness on the velocity profile. Since the boundary layers become thinner for higher Reynolds numbers, the velocity overshoot is confined to a smaller region close to the end walls. This thinner boundary layer has less effect on the centerplane radial velocity and thus there is less tendency toward flow reversal at the higher Reynolds numbers. The thinner boundary layer for  $Re = 200$  causes a considerable difference in appearance between the  $Re = 50$  and the  $Re = 200$  results, but for  $S = 4$  (fig. 5(b-2)), about one-third of the radial flow is confined to the region between  $Z = 0.8$  and the end wall, which was the same result found for the corresponding  $Re = 50$  case. As before, the only effect of varying  $R_1$  seems to be to cause a slightly thinner boundary layer for the  $R_1 = 5$  cases shown in figures 5(b-3) and (b-4) as compared with the  $R_1 = 10$  cases shown in figures 5(b-1) and (b-2).

The radial velocity distributions for  $Re = 2000$  shown in figure 5(c) continue the same trends discussed previously for the lower Reynolds numbers. For the case shown in figure 5(c-2) again about one-third of the radial flow rate is contained between  $Z = 0.8$  and the chamber end wall for  $R = 5$  and  $S = 4$ .

Some representative tangential-velocity profiles are shown in figure 6. Figure 6(a) illustrates a low Reynolds number case which results in thick boundary layers. Despite this thick boundary layer, the centerplane tangential velocity follows a  $1/R$  variation quite closely over the entire range of  $R$ . This indicates that the flow is close to irrotational at the chamber centerplane. For the  $Re = 2000$  case shown in figure 6(b), the boundary layer is much thinner, and the flow outside the boundary layer is essentially irrotational. Tangential-velocity profiles for the other values of the parameters have this same general behavior, with no velocity overshoots or inflections present.

Figure 7 illustrates the relative radial position  $R/R_1$  at which radial-velocity reversals at the chamber centerplane begin for  $R_1 = 10$ . The point at which this reversal occurs is a function of  $Re$  and  $S$ . With increasing swirl ratio, the radial-

velocity reversal takes place closer to the chamber periphery. The reversal is retarded by higher Reynolds numbers due to the resultant thinner boundary layers. Reversal begins to take place somewhere in the chamber at  $S = 4$  for  $Re = 50$  and at  $S = 20$  for  $Re = 200$ , while for  $Re = 2000$  no reversal occurs, even for  $S = 50$ . Results for  $R_1 = 5$  would appear much the same as those shown in figure 7, but all points would be lowered slightly since flow reversal would have less tendency to occur due to the slightly thinner boundary layers that result for the  $R_1 = 5$  cases.

The pressure distribution results are shown in figures 8 and 9. Figure 8 shows dimensionless pressure as a function of relative radial position  $R/R_1$  for swirl ratios greater than 1. For this range of swirl ratios, the predominant factor in the pressure drop is the centrifugal effect, with the frictional pressure drop providing negligible contribution. As a result of this, the single set of curves shown in figure 8 is sufficient to describe the pressure distribution completely independent of  $Re$  and  $R_1$ . The pressure varies strongly along the radius for these swirl ratios as the tangential velocity increases at the expense of the static pressure. The pressure drop becomes essentially infinite as the center of the chamber is approached.

Figure 9 shows the radial pressure distributions for swirl ratios less than 1. In this range, the pressure distribution is a composite of frictional and centrifugal effects. Results are presented for three Reynolds numbers:  $Re = 20$ ,  $200$ , and  $2000$ . The results for  $Re = 20$  shown in figures 9(a) and (b) are somewhat different in shape for  $R_1 = 5$  and  $R_1 = 10$ . For the  $Re = 200$  and  $Re = 2000$  cases shown in figures 9(c) and (d), the same set of curves results for both  $R_1 = 5$  and  $R_1 = 10$ , indicating that  $R_1$  dependence is important only for small  $Re$ . Therefore, in figures 9(c) and (d), the pressure distributions have been plotted as a function of  $R/R_1$ . To give some idea of the effect of adding swirl to the flow, the increase in  $S$  from 0 to 1 gives an increase in the pressure drop at  $R/R_1 = 0.2$  ranging from about 25 percent for the  $Re = 20$ ,  $R_1 = 10$  case shown in figure 9(b) to almost 100 percent for the  $Re = 2000$  case shown in figure 9(d).

Since the experimental work of Savino and Keshock (ref. 4) was for a turbulent flow situation, no direct comparisons with the present analysis can be made. Qualitative comparisons can be made however, and the experimental results for the radial velocity distributions show the same tendency toward a high radial velocity overshoot close to the end wall which increases in magnitude with decreasing radius. These experimental results were obtained for a swirl ratio of about 15. All the experimental profiles show small radial outflow at or near the chamber centerplane, and the results obtained in the present investigation also show a tendency to flow reversal, particularly for high swirl ratios. The tangential velocities near the chamber centerplane in both the experimental work and the present analysis increase with decreasing radius with close to a  $1/R$  variation. This variation is essentially that of an irrotational vortex. The depression

in the tangential-velocity profiles near the chamber centerplane, which was noted in the experimental work, does not occur in the present analysis since this effect occurs only in the presence of significant radial outflow.

## CONCLUSIONS

The laminar, incompressible, viscous flow in a short cylindrical vortex chamber was analyzed numerically. The flow was assumed to enter the chamber with an arbitrary swirl ratio and to exit through a line sink at the chamber axis. The results may be summarized as follows:

1. A velocity overshoot occurred in the radial velocity distribution close to the end wall of the chamber. This overshoot increased with increasing swirl ratio and decreasing radius.
2. The radial velocity at the chamber centerplane decreased with decreasing radius and tended to become negative. This effect was strengthened with increasing swirl ratio.
3. The boundary-layer thickness on the chamber end walls increased with decreasing Reynolds number and tended to weakly increase with increasing dimensionless chamber radius.
4. The tangential flow pattern outside the end-wall boundary layers was essentially an irrotational vortex.
5. The radial pressure variation could be adequately found by assuming the flow to be frictionless and the vortex to be irrotational as long as the swirl ratio was greater than 1.
6. For swirl ratios less than or equal to 1, both swirl and viscous effects made significant contributions to the radial pressure drop.

Lewis Research Center,

National Aeronautics and Space Administration,

Cleveland, Ohio, November 27, 1968,

129-01-05-20-22.

## APPENDIX - SYMBOLS

<b>A, B, F, G</b>	coefficients defined in matrix eq. (20)
<b>h</b>	chamber half-height
<b>P</b>	dimensionless pressure, $(p - p_1)/\rho u_1^2$
<b>p</b>	pressure
<b>p<sub>1</sub></b>	pressure at peripheral inlet of chamber
<b>Q</b>	constant defined in eq. (20)
<b>R</b>	dimensionless radius, $r/h$
<b>Re</b>	Reynolds number, $\rho u_1 h/\mu$
<b>R<sub>1</sub></b>	dimensionless outer radius of chamber, $r_1/h$
<b>r</b>	radial coordinate
<b>r<sub>1</sub></b>	radius of chamber
<b>S</b>	swirl ratio, $v_1/u_1$
<b>U</b>	dimensionless radial velocity, $u/u_1$
<b>u</b>	radial velocity component
<b>u<sub>1</sub></b>	radial inlet velocity at chamber periphery
<b>V</b>	dimensionless tangential velocity, $v/u_1$
<b>v</b>	tangential velocity component
<b>v<sub>1</sub></b>	tangential inlet velocity at chamber periphery
<b>W</b>	dimensionless axial velocity, $w/u_1$
<b>w</b>	axial velocity component
<b>Z</b>	dimensionless axial coordinate, $z/h$
<b>z</b>	axial coordinate
<b><math>\alpha, \beta, \gamma</math></b>	coefficients defined in eq. (20)
<b><math>\Delta R</math></b>	radial finite difference mesh
<b><math>\Delta Z</math></b>	axial finite difference mesh
<b><math>\varphi</math></b>	coefficient defined in eq. (20)
<b><math>\rho</math></b>	density
<b><math>\mu</math></b>	viscosity

Subscripts:

- j denotes radial ( $R$ ) location in finite difference grid; those quantities having subscript  $j$  are known, those with subscript  $j + 1$  are unknown
- k denotes axial ( $Z$ ) location in finite difference grid;  $k = 0$  is chamber centerplane
- n denotes axial location one step ( $\Delta Z$ ) removed from channel end wall; channel end wall is at  $k = n + 1$

## REFERENCES

1. Anderson, Olof L.: Numerical Solutions of the Compressible Boundary Layer Equations for Rotating Axisymmetric Flows. Ph.D. Thesis, Rensselaer Polytechnic Inst., 1966.
2. Donaldson, Coleman duP.; and Snedeker, Richard S.: Experimental Investigation of the Structure of Vortices in Simple Cylindrical Vortex Chambers. Rept. No. 47, Aeron. Res. Assoc. of Princeton, Inc., Dec. 1962.
3. Loper, David E.; and Ostrach, Simon: Analysis of Confined Magnetohydrodynamic Vortex Flows. Phys. Fluids, vol. 11, no. 7, July 1968, pp. 1450-1465.
4. Savino, Joseph M.; and Keshock, Edward G.: Experimental Profiles of Velocity Components and Radial Pressure Distributions in a Vortex Contained in a Short Cylindrical Chamber. NASA TN D-3072, 1965.
5. Bodoia, J. R.; and Osterle, J. F.: Finite Difference Analysis of Plane Poiseuille and Couette Flow Developments. Appl. Sci. Res., Sec. A, vol. 10, 1961, pp. 265-276.
6. Hornbeck, Robert W.; Rouleau, Wilfred T.; and Osterle, Fletcher: Effect of Radial Momentum Flux on Flow in the Entrance of a Porous Tube. J. Appl. Mech., vol. 32, no. 1, Mar. 1965, pp. 195-197.
7. Hornbeck, Robert W.: The Entry Problem in Pipes with Porous Walls. Ph.D. Thesis, Carnegie Institute of Technology, 1961.
8. Hornbeck, Robert W.: Non-Newtonian Laminar Flow in the Inlet of a Pipe. Paper No. 65-WA/FE-4, ASME, 1965.
9. Moller, P. S.: Radial Flow Without Swirl Between Parallel Discs. Aeron. Quart., vol. 14, pt. 2, May 1963, pp. 163-186.
10. Comolet, Raymond: Flow of a Liquid Between Two Parallel Planes. Publ. Sci. and Tech. 334, Ministère de l'Air, France, Sept. 1957, p. 23.
11. Livesey, J. L.: Inertia Effects in Viscous Flow. Int. J. Mech. Eng. Sci., vol. 1, no. 1, Jan. 1960, pp. 84-88.
12. Peube, J. L.: Sur l'Écoulement Radial Permanent d'un Fluide Visqueux Incompressible Entre Deux Plans Parallèles Fixes. J.de. Méchanique, vol. 2, no. 4, Dec. 1963, pp. 377-395.

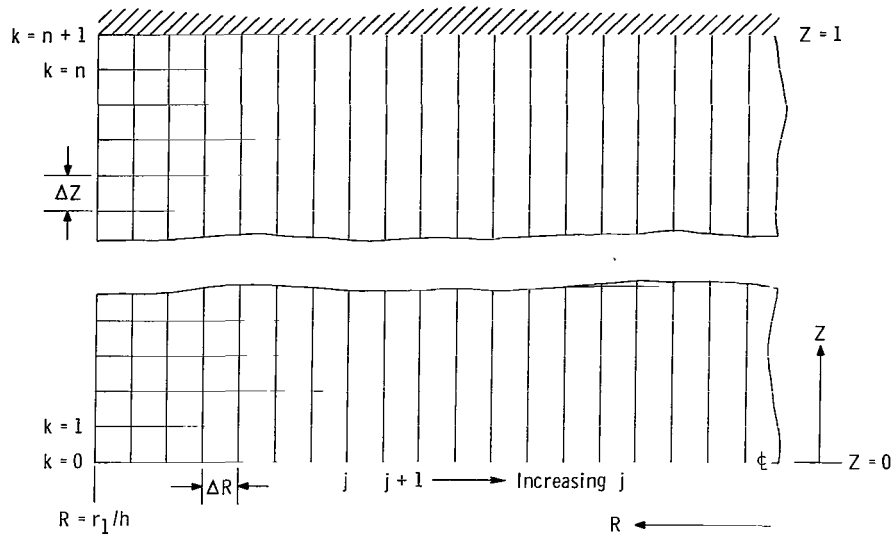


Figure 2. - Finite difference grid.

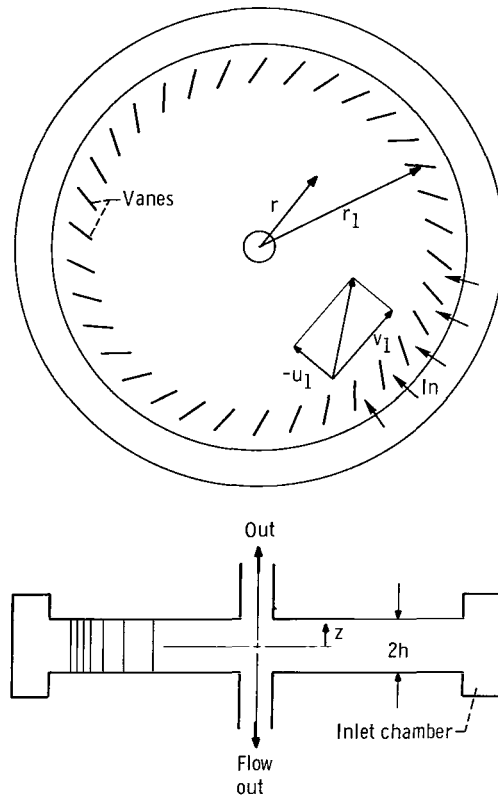
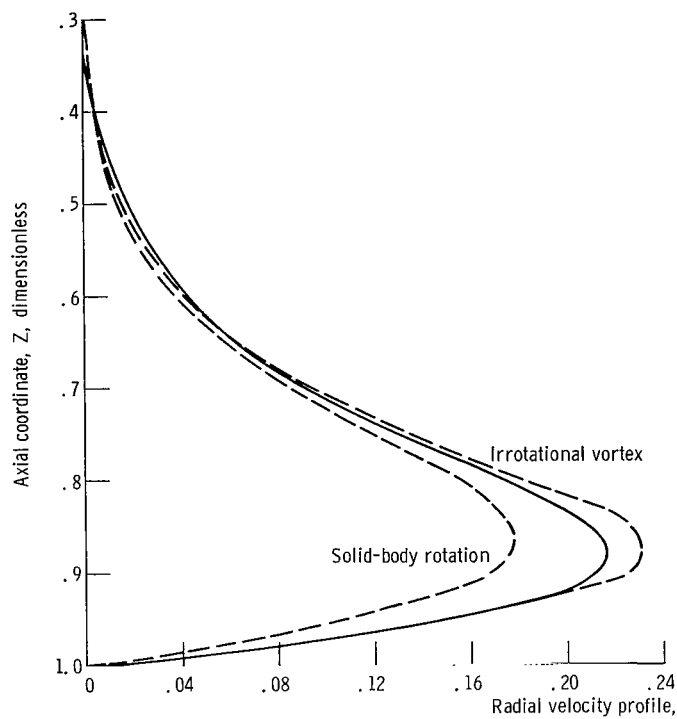
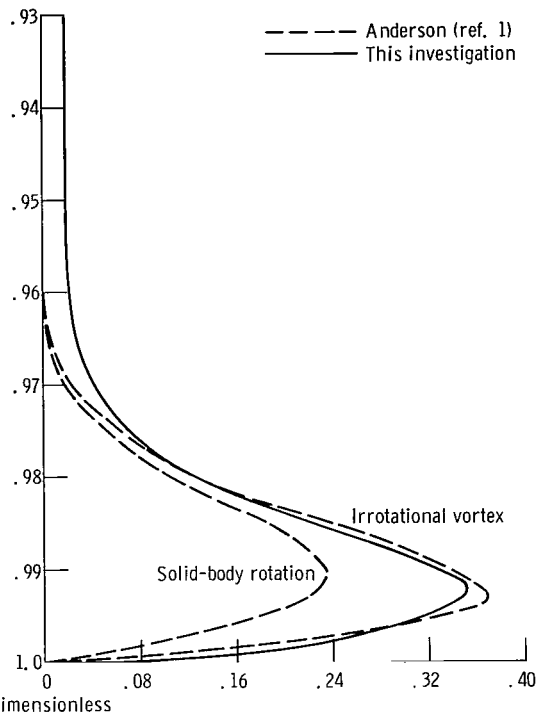


Figure 1. - Typical short-vortex chamber configuration.



(a) Reynolds number, 15; swirl ratio, 20; dimensionless radius, 9.



(b) Reynolds number, 2000; swirl ratio, 50; dimensionless radius, 8.

Figure 3. - Comparison of radial velocity profile with those of reference 1. Dimensionless chamber radius 10.



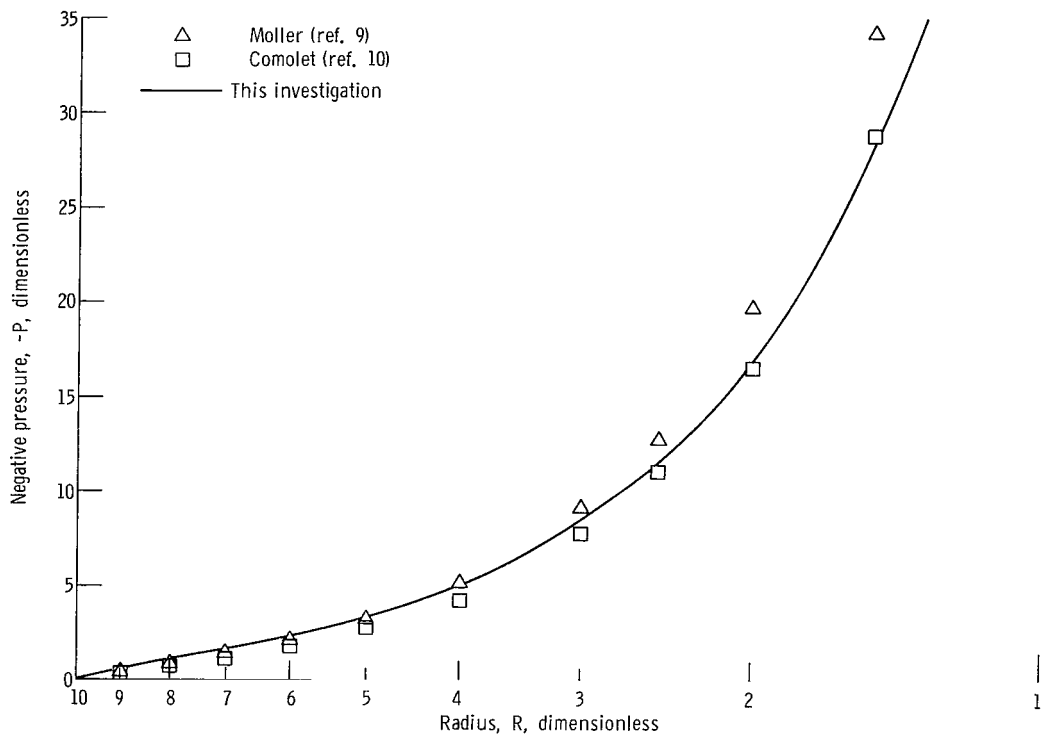
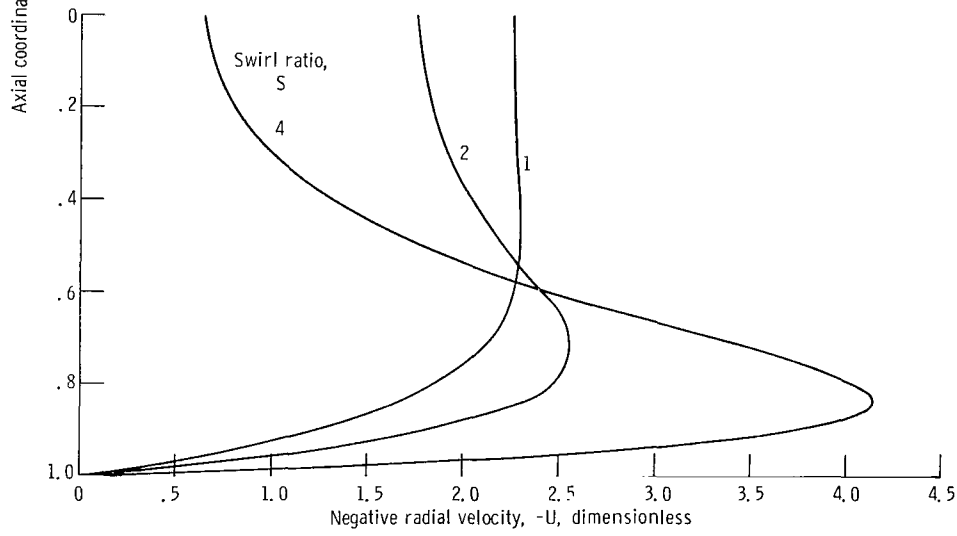
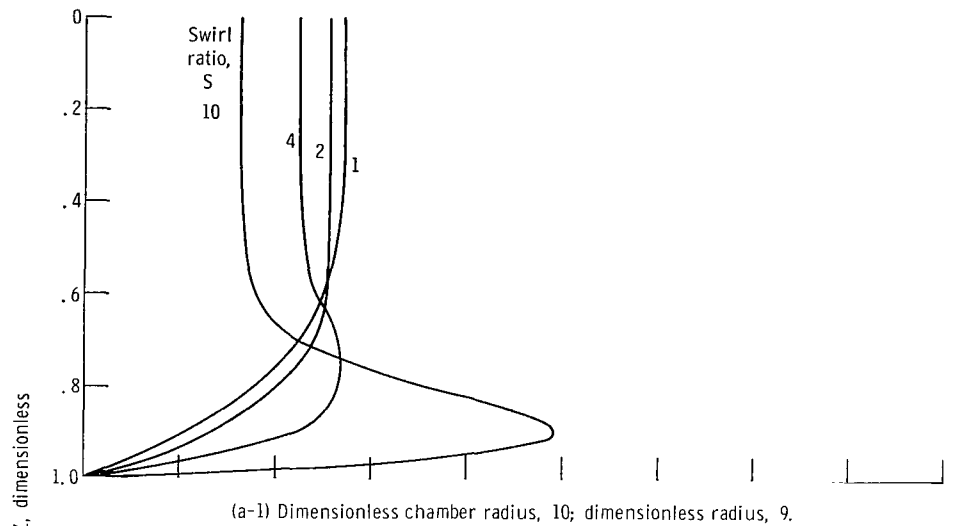
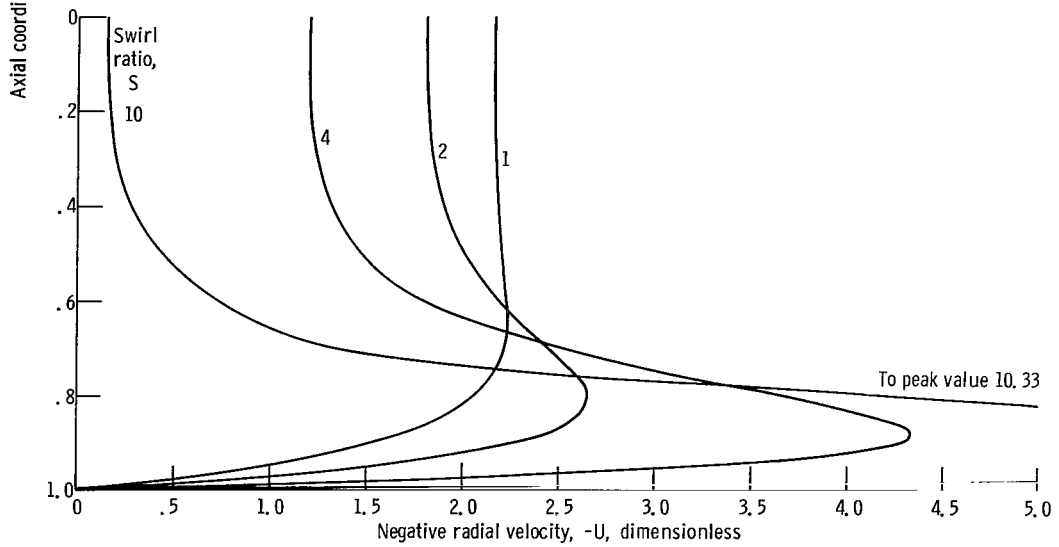
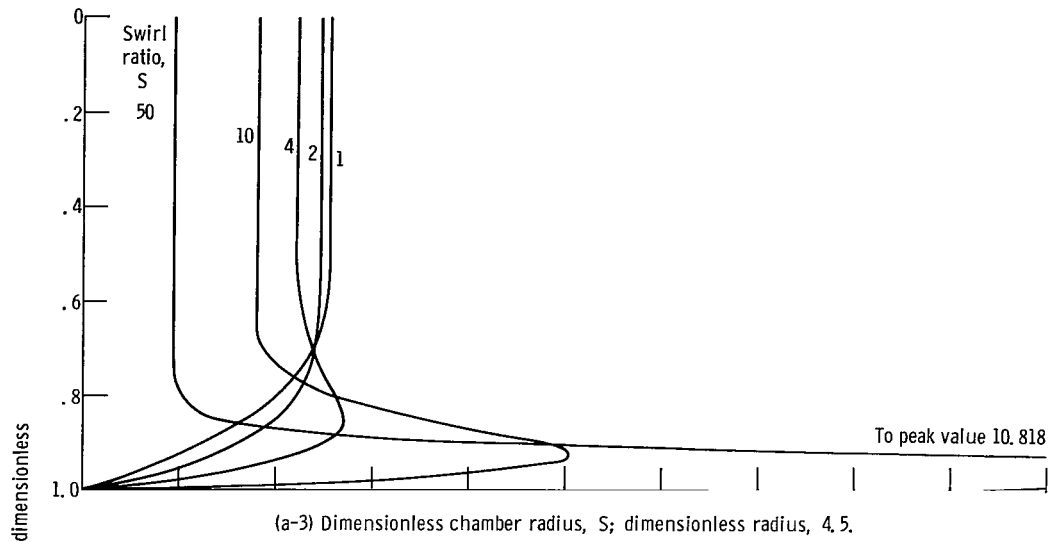


Figure 4. - Comparison of radial pressure distributions for zero swirl. Reynolds number, 20; swirl ratio, 0; dimensionless chamber radius, 10.



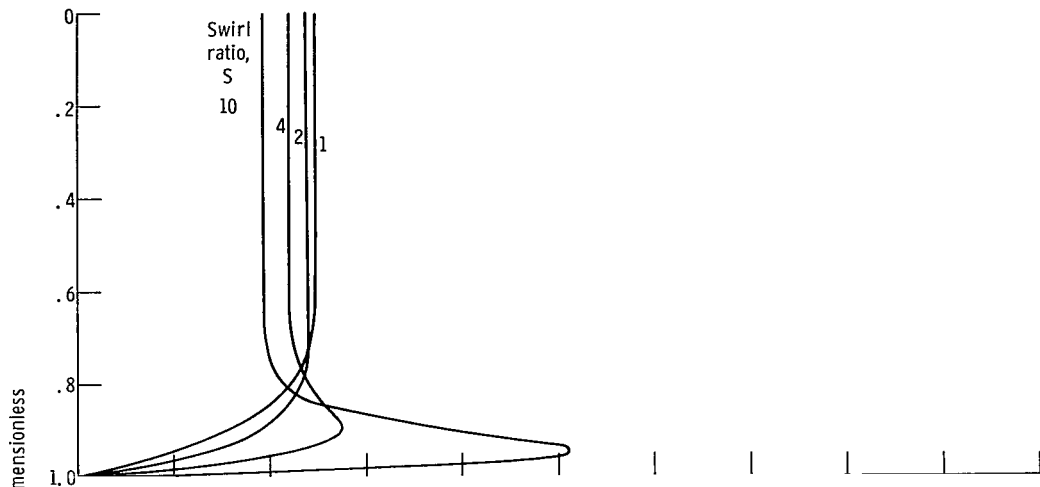
(a) Reynolds number, 50.

Figure 5. - Radial velocity profiles.

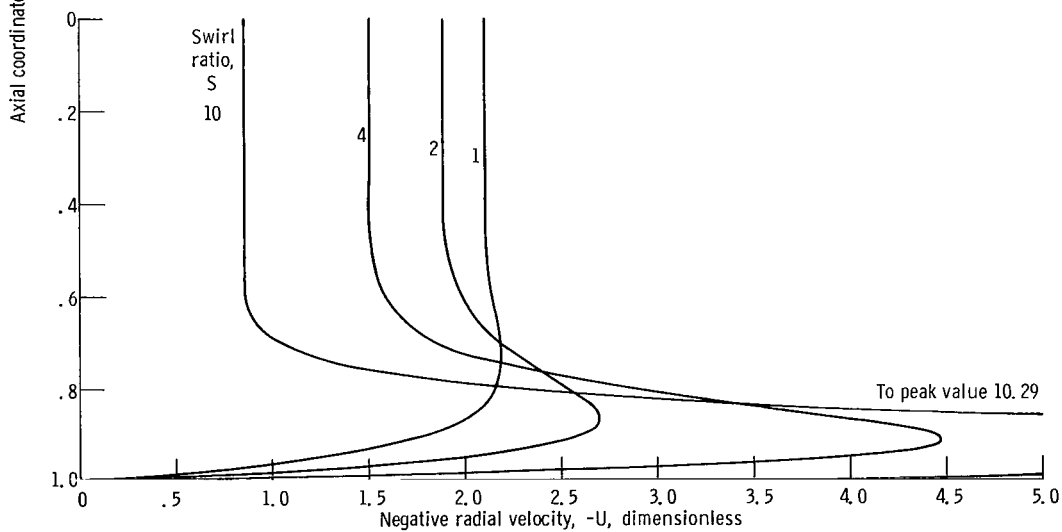


(a) Concluded.

Figure 5. - Continued.



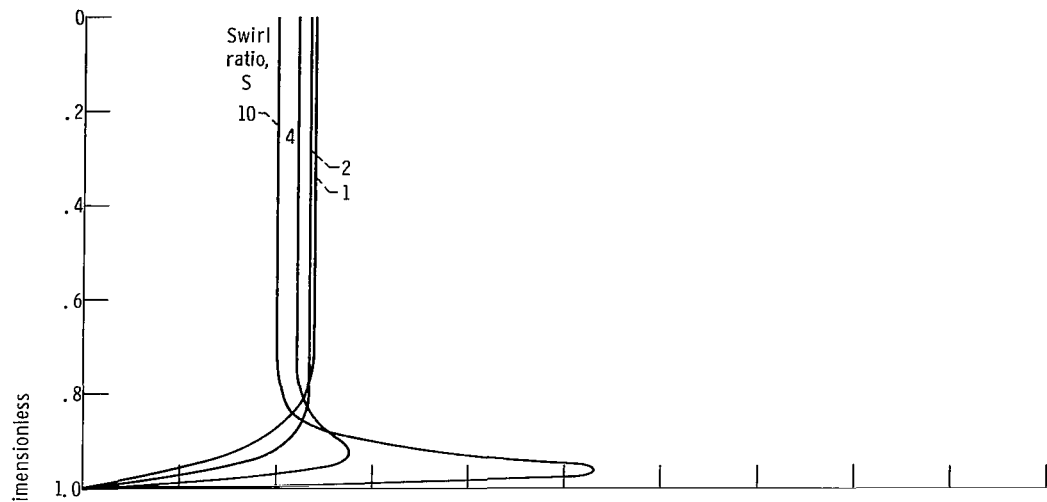
(b-1) Dimensionless chamber radius, 10; dimensionless radius, 9.



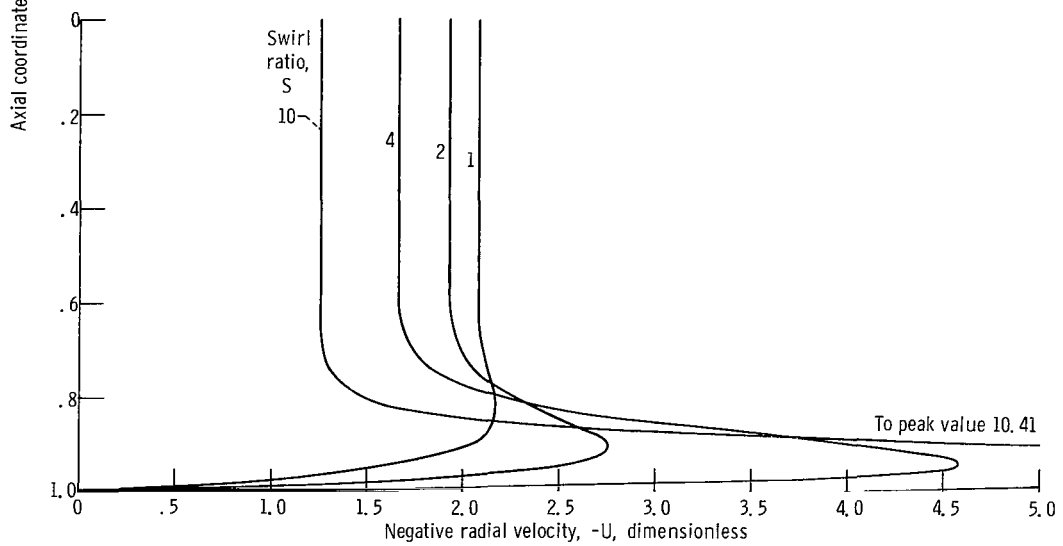
(b-2) Dimensionless chamber radius, 10; dimensionless radius, 5.

(b) Reynolds number, 200.

Figure 5. - Continued.



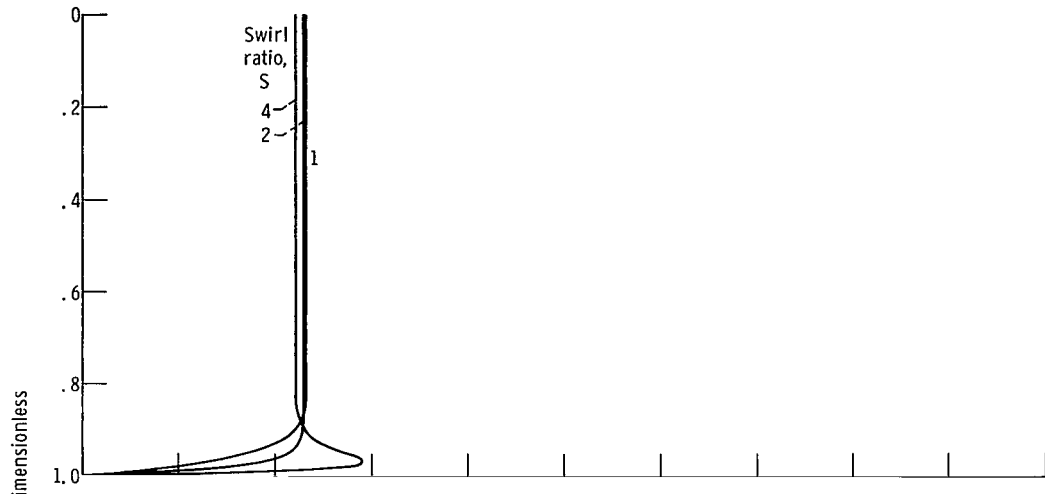
(b-3) Dimensionless chamber radius, 5; dimensionless radius, 4.5.



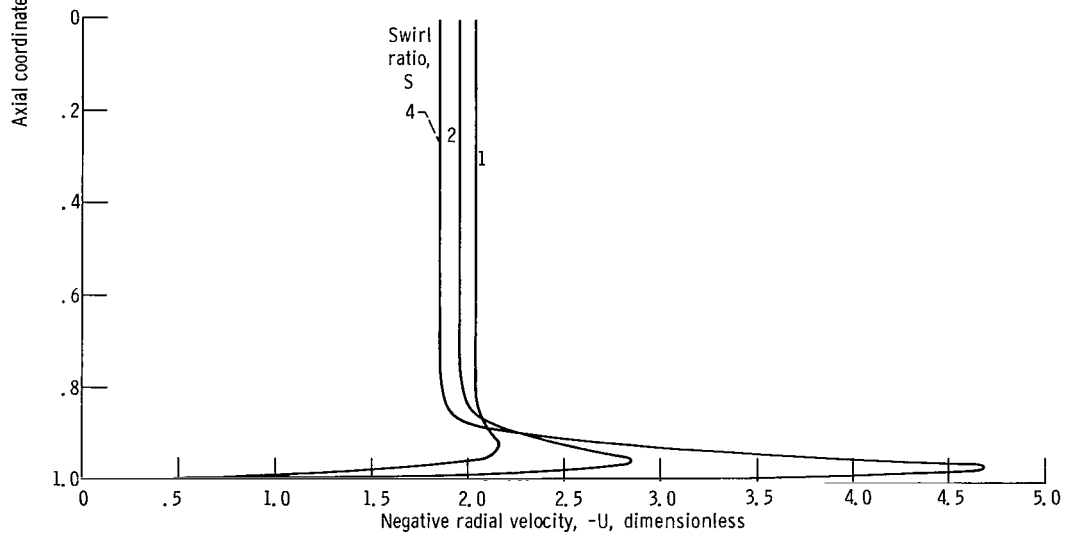
(b-4) Dimensionless chamber radius, 5; dimensionless radius, 2.5.

(b) Concluded.

Figure 5. - Continued.



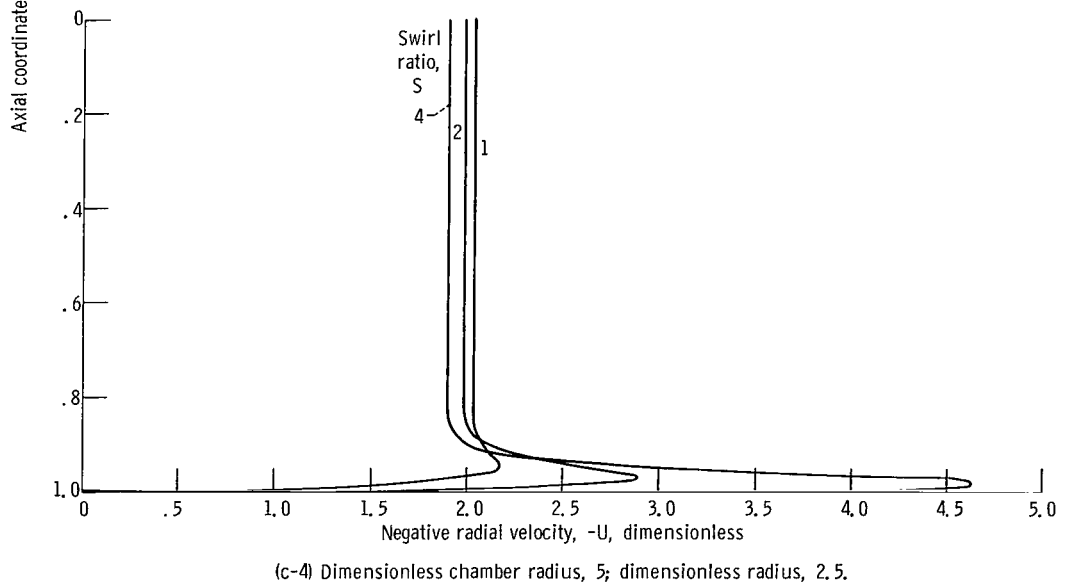
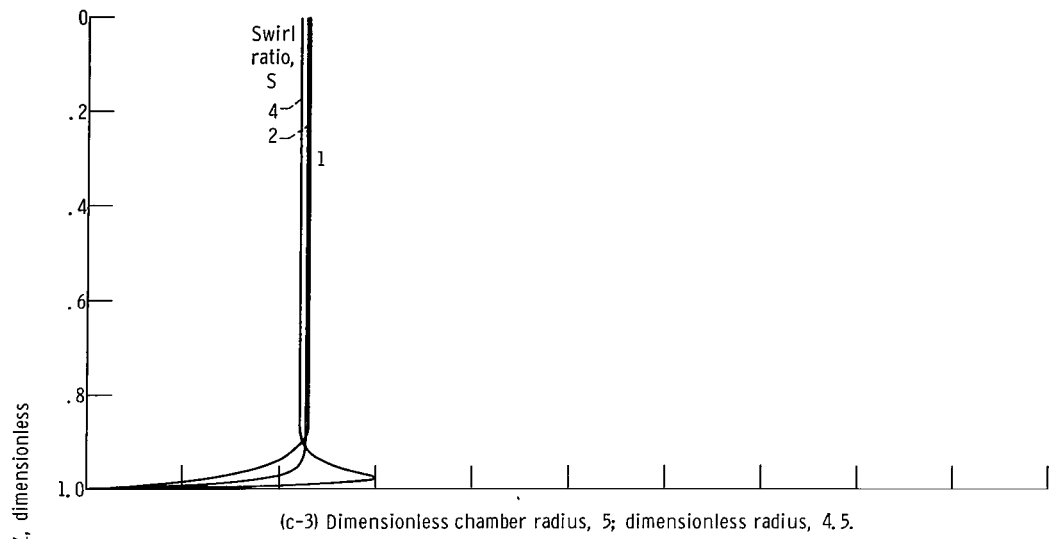
(c-1) Dimensionless chamber radius, 10; dimensionless radius, 9.



(c-2) Dimensionless chamber radius, 10; dimensionless radius, 5.

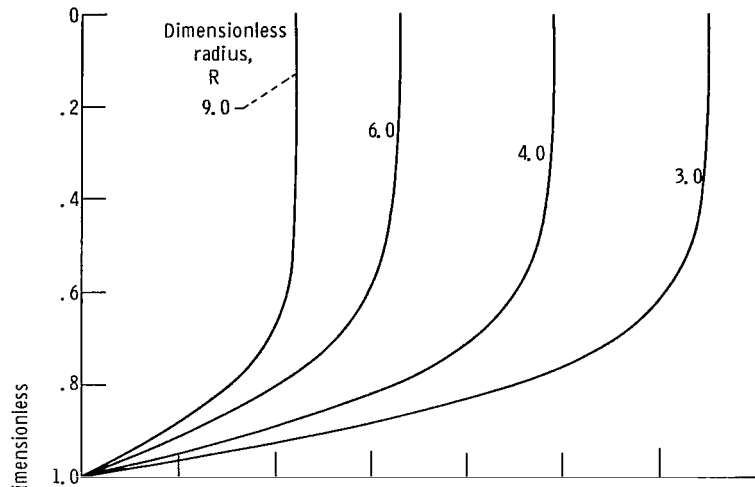
(c) Reynolds number, 2000.

Figure 5. - Continued.

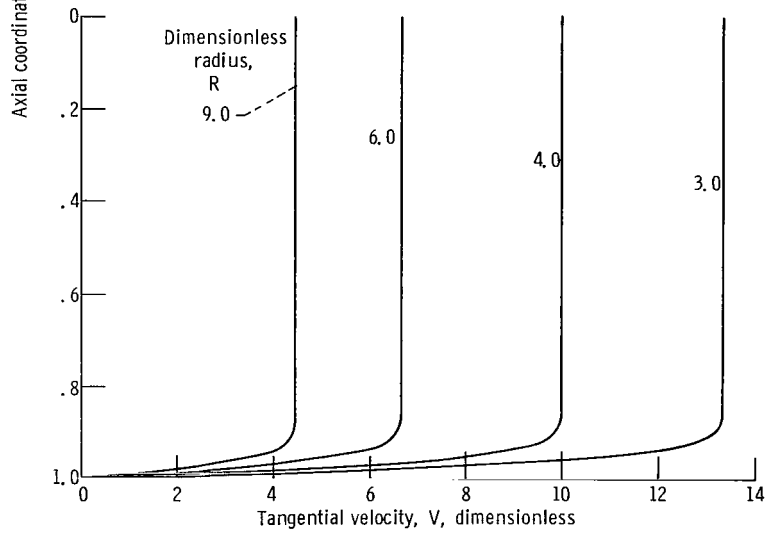


(c) Concluded.

Figure 5. - Concluded.



(a) Reynolds number, 50.



(b) Reynolds number, 2000.

Figure 6. - Tangential velocity profiles. Dimensionless chamber radius, 10; swirl ratio, 4.



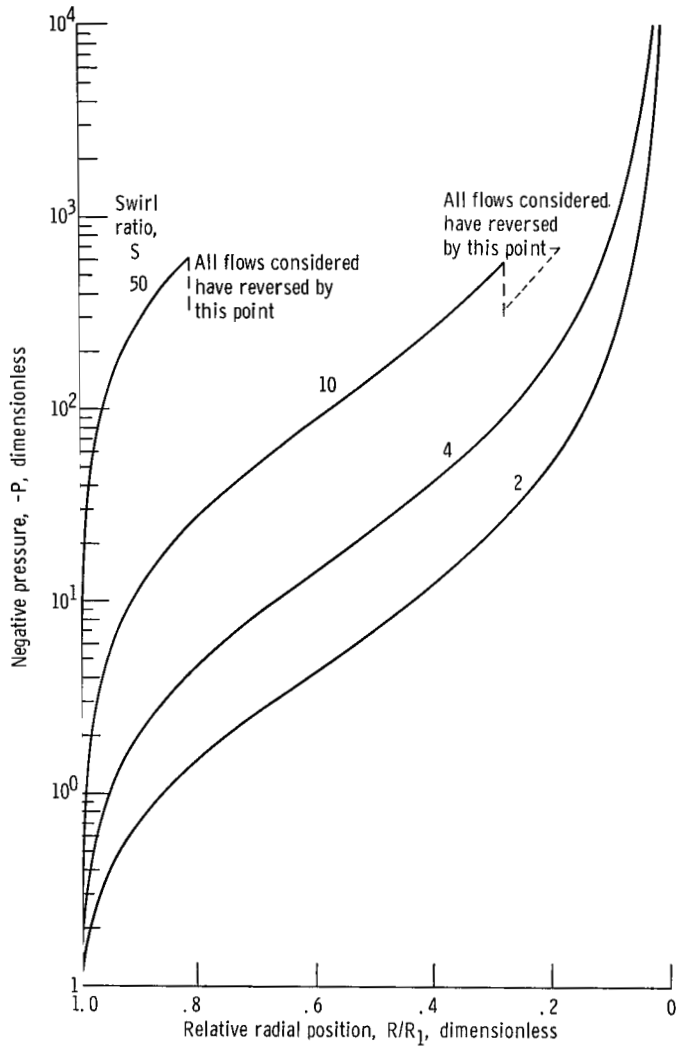


Figure 8. - Radial-pressure distributions for high swirl.

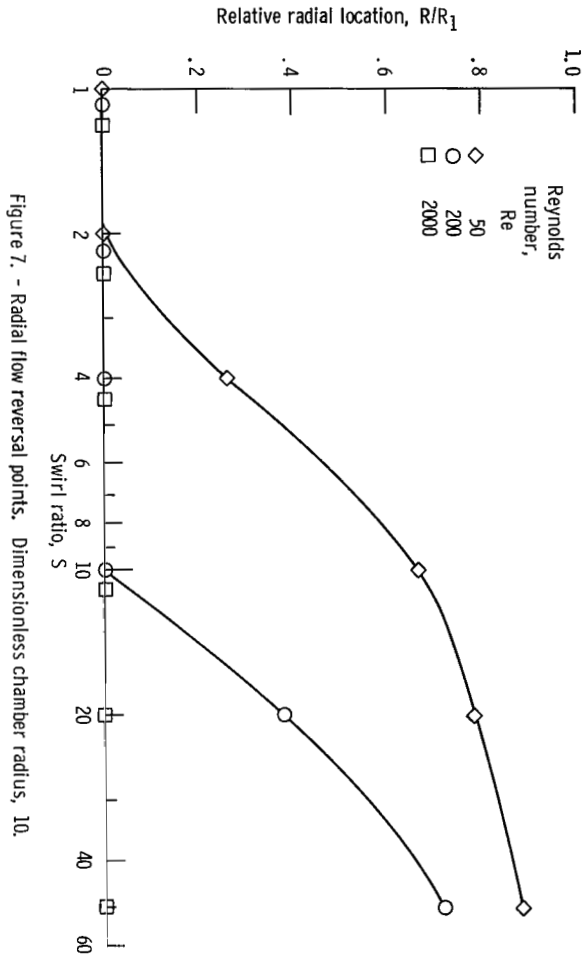
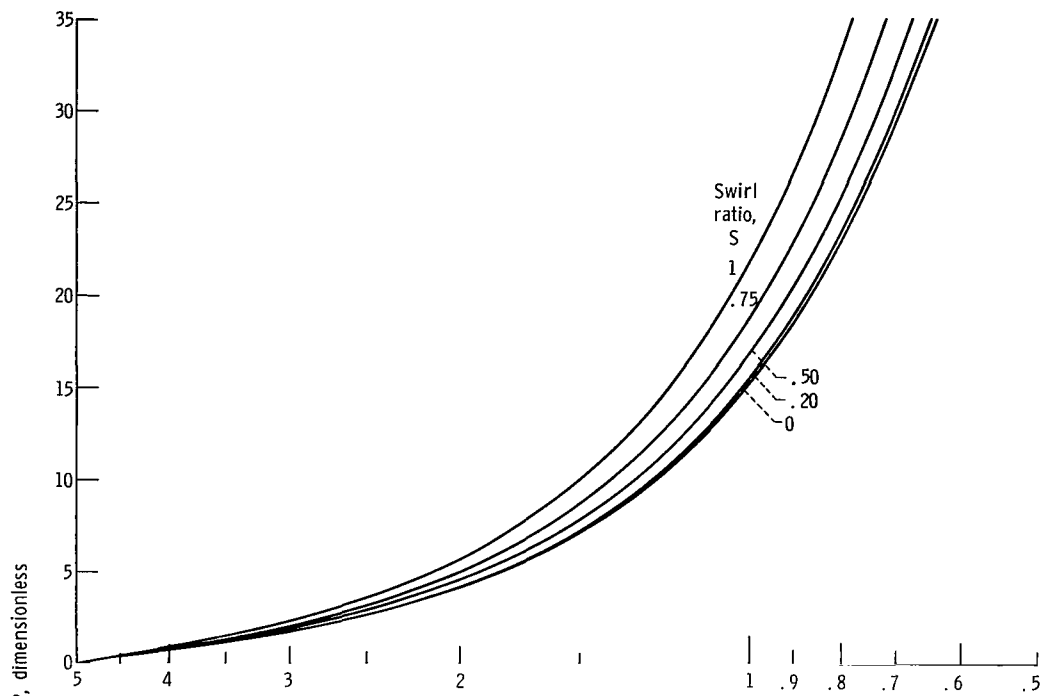
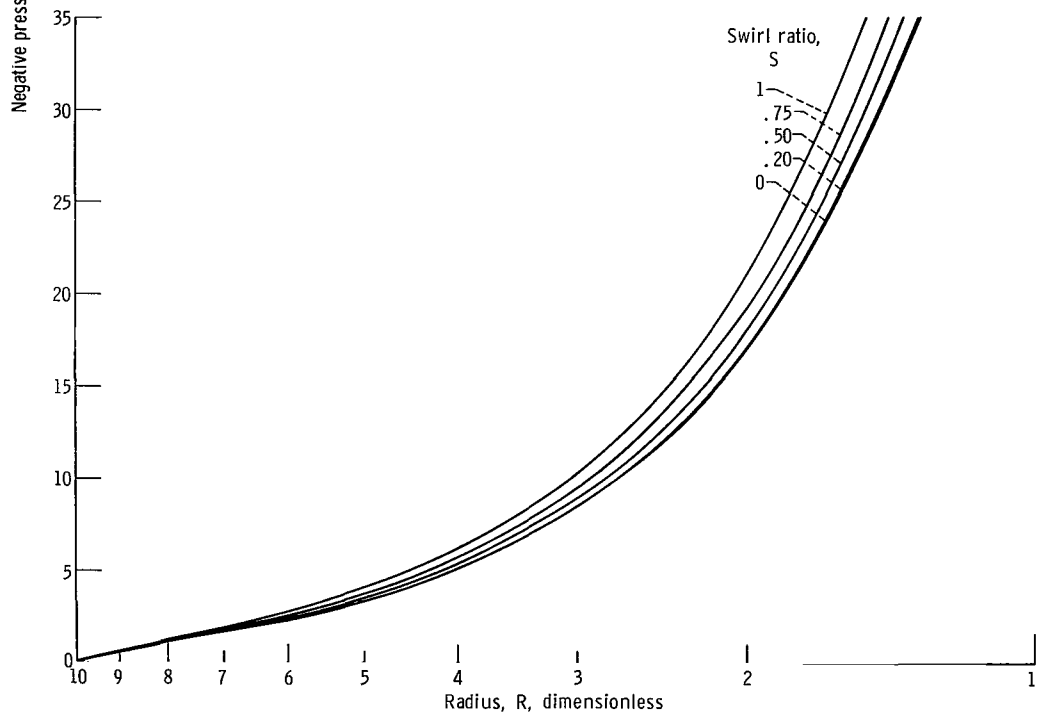


Figure 7. - Radial flow reversal points. Dimensionless chamber radius, 10.



(a) Reynolds number, 20; dimensionless chamber radius, 5.



(b) Reynolds number, 20; dimensionless chamber radius, 10.

Figure 9. - Continued.

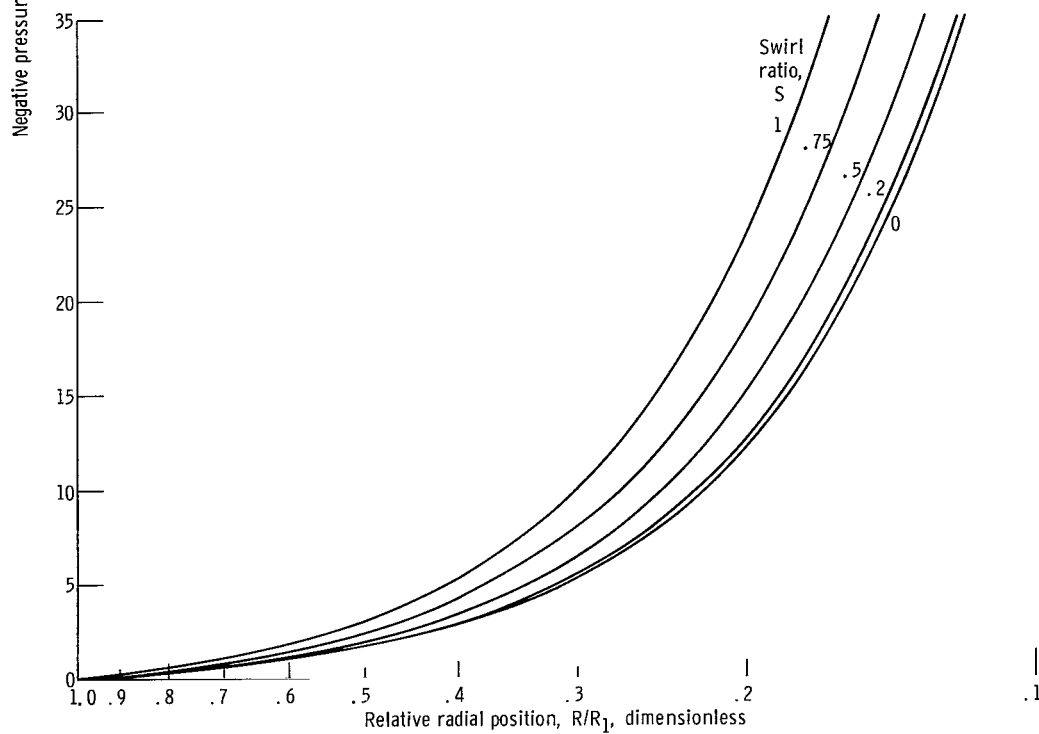
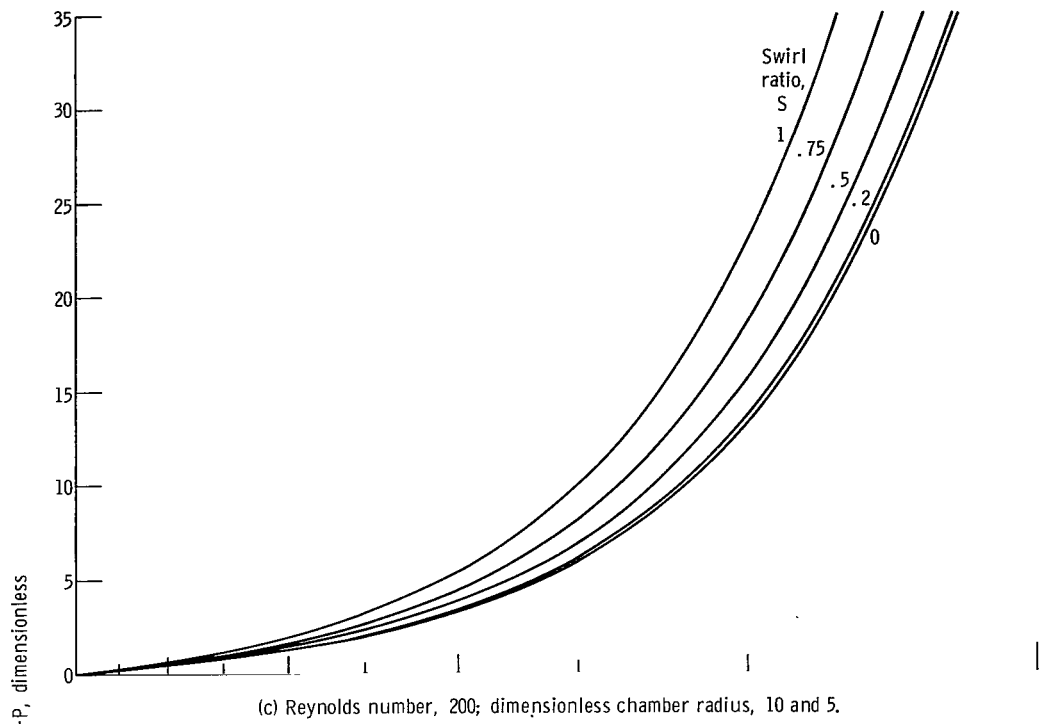


Figure 9. - Concluded.

FIRST CLASS MAIL

POSTMASTER: If Undeliverable (Section 15E  
Postal Manual) Do Not Return

*"The aeronautical and space activities of the United States shall be conducted so as to contribute . . . to the expansion of human knowledge of phenomena in the atmosphere and space. The Administration shall provide for the widest practicable and appropriate dissemination of information concerning its activities and the results thereof."*

— NATIONAL AERONAUTICS AND SPACE ACT OF 1958

## NASA SCIENTIFIC AND TECHNICAL PUBLICATIONS

**TECHNICAL REPORTS:** Scientific and technical information considered important, complete, and a lasting contribution to existing knowledge.

**TECHNICAL NOTES:** Information less broad in scope but nevertheless of importance as a contribution to existing knowledge.

**TECHNICAL MEMORANDUMS:** Information receiving limited distribution because of preliminary data, security classification, or other reasons.

**CONTRACTOR REPORTS:** Scientific and technical information generated under a NASA contract or grant and considered an important contribution to existing knowledge.

**TECHNICAL TRANSLATIONS:** Information published in a foreign language considered to merit NASA distribution in English.

**SPECIAL PUBLICATIONS:** Information derived from or of value to NASA activities. Publications include conference proceedings, monographs, data compilations, handbooks, sourcebooks, and special bibliographies.

**TECHNOLOGY UTILIZATION PUBLICATIONS:** Information on technology used by NASA that may be of particular interest in commercial and other non-aerospace applications. Publications include Tech Briefs, Technology Utilization Reports and Notes, and Technology Surveys.

*Details on the availability of these publications may be obtained from:*

**SCIENTIFIC AND TECHNICAL INFORMATION DIVISION  
NATIONAL AERONAUTICS AND SPACE ADMINISTRATION  
Washington, D.C. 20546**